Regular modes in a mixed-dynamics-based optical fiber

Claire Michel, Markus Allgaier, Valérie Doya

Regular modes in a mixed-dynamical based optical fiber

C. Michel,[1] M. Allgaier[1,2] and V. Doya[1]
[1] *Laboratoire de Physique de la Matière Condensée, CNRS UMR 7336, Université Nice-Sophia Antipolis, 06100 Nice, France*
[2] *Integrated Quantum Optics, Applied Physics, University of Paderborn, 33098 Paderborn, Germany*

A multimode optical fiber with a truncated transverse cross section acts as a powerful versatile support to investigate the wave features of complex ray dynamics. In this paper, we concentrate on the case of a geometry inducing mixed dynamics. We highlight that regular modes associated to stable periodic orbits present an enhanced spatial intensity localization. We report the statistics of the Inverse Participation Ratio whose features are analogous to those of Anderson localized modes. Our study is supported both by numerical and experimental results on the spatial localization and spectral regularity of the regular modes.

PACS numbers: 05.45.Mt, 42.81.Wg

I. INTRODUCTION

Mixed-dynamical based systems are more and more used in applications, especially in optics [1]. These systems, whose geometry induces complex ray dynamics, bring a new kind of solutions for practical purposes through their singular wave properties [2]. The common attribute of mixed systems is the coexistence of both chaotic and regular dynamics leading to a large wealth for the corresponding wave behavior (wave chaos). This duality manifests itself on the spatial properties of the modes by exhibiting on the one hand a generic statistically uniform distribution, that is ergodicity [3], and on the other hand specific patterns along regular trajectories [4]. Dielectric microcavities stand as the typical example of the exploitation of wave chaos as an improvement of existing devices. Indeed, microcavity lasers with mixed geometry allow low threshold and highly directional outputs [5, 6] and are a very useful solution for integrated optics. Recently, microcavity-based gyroscopes in which a deformed cavity enhances the rotation sensitivity [7] have been investigated. The ergodic/regular twofold feature gives also rise to much more subtle phenomena. As an illustration, a diffractive free regime of light propagation has been observed in a segmented optical waveguide presenting a mixed ray dynamics [8]. In this case, the absence of diffraction results from the superposition of modes constructing on a stable periodic trajectory. Moreover, dynamical tunneling, namely a passage between the chaotic and regular regions by coupling one to another [9–12], is one of the main manifestation of this duality. This effect has been used in deformed microdisks in which light is coupled to a bus waveguide through the tunneling effect acting as a resonant dynamical filter [13].

A highly multimode optical fiber whose transverse cross-section presents a truncated-circle shape allows to explore different regimes of the dynamics by changing the size of the truncation (e.g. changing d in Fig. 1(a)). Over the past few years we studied experimentally manifestations of ergodicity as well as deviations from this universal behavior due to scar modes in passive and active fully chaotic optical fibers [14–17]. The ergodicity features of modes in a chaotic fiber have already been proposed as an optimized solution for applications in telecommunications (e.g. in double-clad fiber amplifiers [18–20]). We keep on exploiting the potential of complex-dynamical based multimode optical fibers, but now for mode division multiplexing (MDM) [21]. In this context we show that a mixed optical fiber presents singular wave features allowing the control of individual modes in a highly multimode system.
In this paper, we report an exhaustive study on the properties of the modes of a mixed-dynamics based multimode optical fiber, and in particular modes that are associated to the regular part of the dynamics. These *regular modes* present strong spatial and spectral signatures through a localization of the field along stable trajectories and a regularly distributed spectrum respectively. This localization is triggered by the stability of the dynamics and is studied by means of the Inverse Participation Ratio and its statistics. We show that, unlike ergodic modes whose statistics follow a universal behavior, the regular modes induce some deviations that are analogous to those resulting from localized modes in disordered systems [22]. We present a characteristic structuring of the IPR with respect to modes families that makes them easily traceable. We use an analysis based on Gaussian beams in cavity in order to analytically describe the structuring of the IPR for the regular modes.

In a context of a growing exploitation of multimode fibers – in telecommunications devices as well as in imaging processes – both description and control of individual modes are of great importance. This study reports on a detailed analysis of highly distinguishable modes with singular spatial and spectral properties. We develop an experiment that, based on these modes features, allow us to isolate them among thousands of modes. These results exalt the ability of the regular modes to be used as individual communication channels.

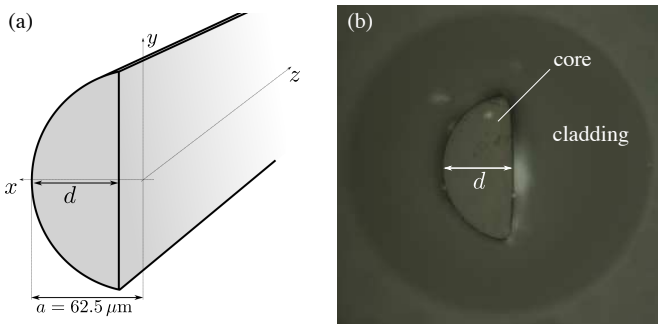

FIG. 1. Presentation of the experimental system. (a) scheme of the fiber with $\gamma < 1$, (b) picture of the cross section of the optical fiber for $\gamma = 0.95$ taken with a standard microscope in the transmission mode

Protected from other modes by the stability of the dynamics, they may offer a solution to prevent mode coupling in MDM.

In section II, we present our experimental system and its main geometrical and modal characteristics specifically its localization features. In section III, we develop the analysis of the spatial properties of the regular modes of the fiber using the analogy with the Gaussian modes of an optical resonator. In section IV we propose a characterization of the spatial localization of the modes through tools commonly used to measure deviations from a uniform distribution (i.e. the Inverse Participation Ratio) and we point out a way to distinguish specific family of regular modes. A spectral analysis of the regular modes of the optical fiber based on an experimental selective excitation and on numerical results is reported in section V. Then, in section VI, we conclude and suggest some potential applications in an open discussion.

II. THE OPTICAL FIBER AS A VERSATILE OPTICAL COUNTERPART OF A DYNAMICAL SYSTEM

Our experimental system is a non-standard silica multimode optical fiber, whose cross section is a truncated disk. The length of the fiber is 10cm, the diameter of its core is $2a = 125\mu$m. The truncated diameter is denoted $d = \gamma\, a$, with $\gamma \in]0\,;2]$. The core is surrounded by a silicon cladding of diameter 250μm [Fig. 1(b)]. The optical indexes are $n_{\rm co} = 1.458$ and $n_{\rm cl} = 1.41$ for the core and the cladding respectively at the vacuum wavelength $\lambda_0 = 632$nm. As the wavelength is small compared to the characteristic size a of our system, one can consider a semiclassical approach. The longitudinal evolution of a ray along the fiber (a three-dimensional system) is formally equivalent to the time evolution of a trajectory in the transverse cross-section of the fiber. It is thus analogous to a two-dimensional (2D) bounded cavity which is a well-known paradigm of a Hamiltonian dynamical system (2D billiard) [2]. In the following, we will consider the propagation modes of the fiber as the modes of a 2D cavity and thus refer to the transverse cross section of the optical fiber as a "cavity". It is worth mentioning that an optical fiber is a very low lossy system, and as we restrict our study to less than the first third of the total number of modes, the approximation of a closed system is valid.

The versatility of our system relies on its ability to explore different types of dynamics from regular to chaotic by varying the factor γ. The qualification of the dynamics is commonly studied through a stroboscopic phase-space representation, well-known as the Poincaré Surface of Section (PSS). It consists in plotting at each impact of the ray on the boundary the curvilinear abscissa s measured through the angle $\theta = s/a$ and the sine of the incidence angle, α [Fig. 2(a)]. As shown in Fig. 2(c-e) and as pointed out by Ree *et al.* [23], the PSS presents the characteristic behaviors related to different types of dynamics while varying γ. For $0 < \gamma < 1$, the dynamics is mixed and the PSS presents a complex combination of stochastic and regular regions. The optical fiber used in the experiment has a truncated diameter corresponding to $\gamma = 0.95$. In the PSS reported in Figure 2(c) for this value, regular islands coexist with diffuse points associated to the so-called chaotic sea [23, 24]. Each regular island corresponds to quasi-periodic trajectories in the vicinity of a stable periodic orbit (PO) at the center of the island. A large fraction of PSS is occupied by the main central resonance that corresponds to the 2 bounce PO (2-PO). As d reaches the value of the radius a ($\gamma = 1$, half-circle), the PSS testifies of the regular nature of the dynamics [Fig. 2(d)]. In this case, the angle of reflection $|\alpha|$ is conserved for any given initial condition. Note that the PSS of a circular billiard ($\gamma = 2$) has the same aspect due to angle conservation. When d becomes greater than a ($1 < \gamma < 2$), regular islands no longer exist, and all the POs become unstable. Then, the PSS is densely covered by diffuse points and the dynamics is fully chaotic [Fig. 2(e)]. It is worth mentioning that the latter geometry has also been extensively investigated in optical fibers over the past few years [14–17, 25]. In particular, the authors experimentally demonstrated that some specific scarred modes of a chaotic optical fiber – spatially localized along the least unstable periodic orbits – can be selectively enhanced through an optical amplification process [17, 25]. Moreover, as the pump absorption is clearly improved by the use of a chaotic double-clad fiber amplifier, the device has been proposed as an optimization of existing amplifiers [18, 26].

Here, we devote our study to the mixed dynamics, using a D-shaped optical fiber with $\gamma = 0.95$. The length of the fiber is greater than the "Heisenberg length"[14] z_h=8.3cm for which the modes are resolved ensuring the validity of a modal description of light propagation. The number of modes of the fiber is given by the usual formula [27] and is evaluated to approximatively $N = 6000$ at λ_0. The 2000 first modes are calculated numerically using a finite element method. In the paraxial approx-

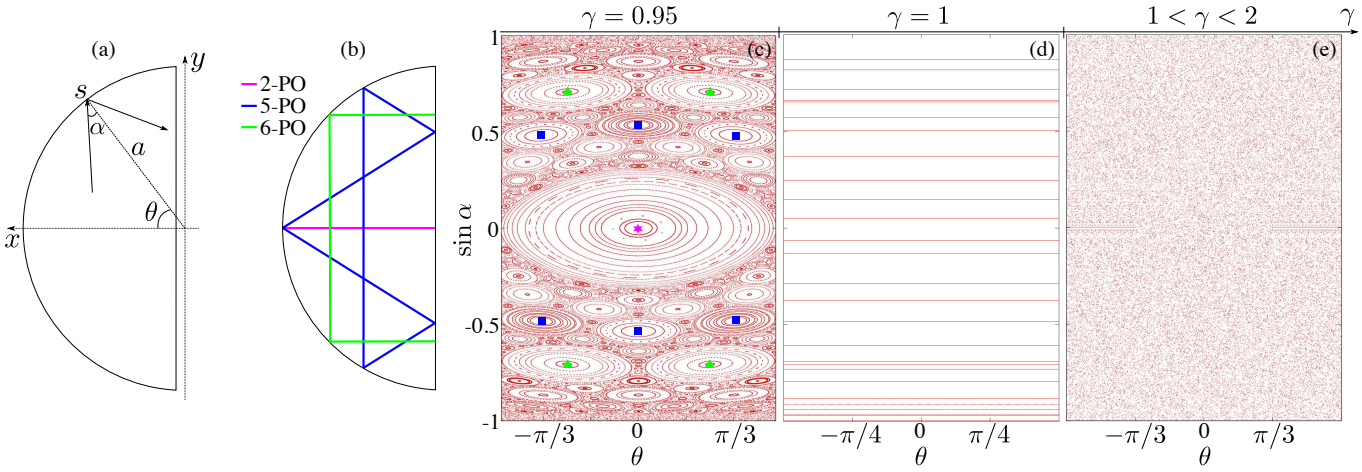

FIG. 2. (a) Curvilinear abscissa $s = a\theta$ and angle of reflection α used for the calculation of the PSS and Husimi representations. (b) Three examples of stable periodic orbits of the mixed billiard ($\gamma = 0.95$) : in pink the 2-PO, in blue the 5-PO and in green the 6-PO.(c)-(e) Poincaré Surface of Section representation for three different values of γ. (c) $\gamma = 0.95$, mixed dynamics with a coexistence of regular and chaotic trajectories ; the pink star points out the 2-bounce stable periodic orbit, the blue squares correspond to the central point of the stability islands of the 6-bounce stable periodic orbit and the green triangles to the 5-bounce stable periodic orbit, (d) $\gamma = 1$, regular dynamics for which one sees the conservation of the angle of reflection, whatever the initial condition is, (e) $\gamma = 2/3$, chaotic dynamics, no stability regions, all the periodic orbits are unstable.

imation, the Hemholtz equation is equivalent to the 2D Schrödinger equation [14]. One thus has access to the spatial distribution of the modes (eigenvectors), as well as their corresponding frequencies (eigenenergies). As shown on four examples in Figure 3, the modes exhibit some signatures of the underlying classical mixed dynamics [28]. The spatial distribution of intensity (near-field, NF) of the mode in Fig. 3(a) is located on the 2-PO represented in pink in Fig. 2(b). Figure 3(b) shows the far-field (FF) of the same mode. The FF is the square modulus of the spatial Fourier transform of the field distribution. It indicates the direction $\vec{\kappa}$ and modulus κ of the transverse wave vectors. For Fig. 3(b), two maxima of intensity are localized along the direction of the 2-PO at at an equal distance κ of the center of the Fourier space. This directivity in the FF evidences the signature of the underlying 2-PO (see Fig. 2). Strong correspondances between some particular modes and their associated classical trajectories in the semiclassical regime are established through the Husimi representation, which is commonly used as a wave equivalent to the classical PSS [29]. In the case of 2D cavities with Dirichlet boundary conditions, the Husimi function is evaluated through the normal derivative of the eigenfunction on the boundaries of the cavity [23, 30–32]. The Husimi function is calculated for the modes of the optical fiber and is represented in the 2D space $(\theta, \sin\alpha)$. Here, $\sin\alpha$ represents the projection of the transverse wave vector $\vec{\kappa}$ along the tangential direction to the boundary, normalized by the modulus $\kappa = |\vec{\kappa}|$ of the mode. Figure 3(c) displays the Husimi representation of the mode shown in Fig. 3(a) with the PSS of the 2-PO superimposed. The localized pattern of the intensity in the Husimi representation means that the mode is strongly confined along the x-direction. This confinement as well as the very good agreement between both this representation and the PSS confirms that this mode builds on constructive interferences along the 2-PO. In the same way, Figures 3(d,e,f) and (g,h,i) show the NF, FF and Husimi representations of modes built in the vicinity of the 5-bounce [Fig. 2(b), blue line] and 6-bounce [Fig. 2(b), green line] stable periodic orbits respectively. As before, the agreement between the Husimi and PSS representation reflects the fact that the ray dynamics is the skeleton of the modal behavior. Figures 3(j,k,l) present the NF, FF and Husimi representations of a chaotic mode of the fiber. The FF is isotropically distributed and the Husimi representation is no longer confined in small areas delimited by the corresponding stability islands of the PSS, but spreads over the chaotic regions.

As conjectured by Percival [28], the duality between chaotic and regular dynamics is also encountered in the spectral features. A simple way to quantify the degree of regularity of a 2D-cavity is given by the study of the statistics of energy level spacing

$$s_{\Delta,n} = \mathcal{N}_{\mathrm{W}}(E_{n+1}) - \mathcal{N}_{\mathrm{W}}(E_n) \tag{1}$$

where E_n is the energy of mode n and $\mathcal{N}_{\mathrm{W}}(E_n)$ the number of modes of energy lower or equal to E_n given by the Weyl formula [33]

$$\mathcal{N}_{\mathrm{W}}(E_n) = \frac{\mathcal{S}}{2\pi}E_n - \frac{\mathcal{P}}{4\pi}\sqrt{2E_n} \tag{2}$$

with $\mathcal{S}$ and $\mathcal{P}$ respectively the surface and perimeter of the cross section of the fiber, and the energies being given by $E_n = \kappa_n^2/2$. As described in [34, 35], the probability

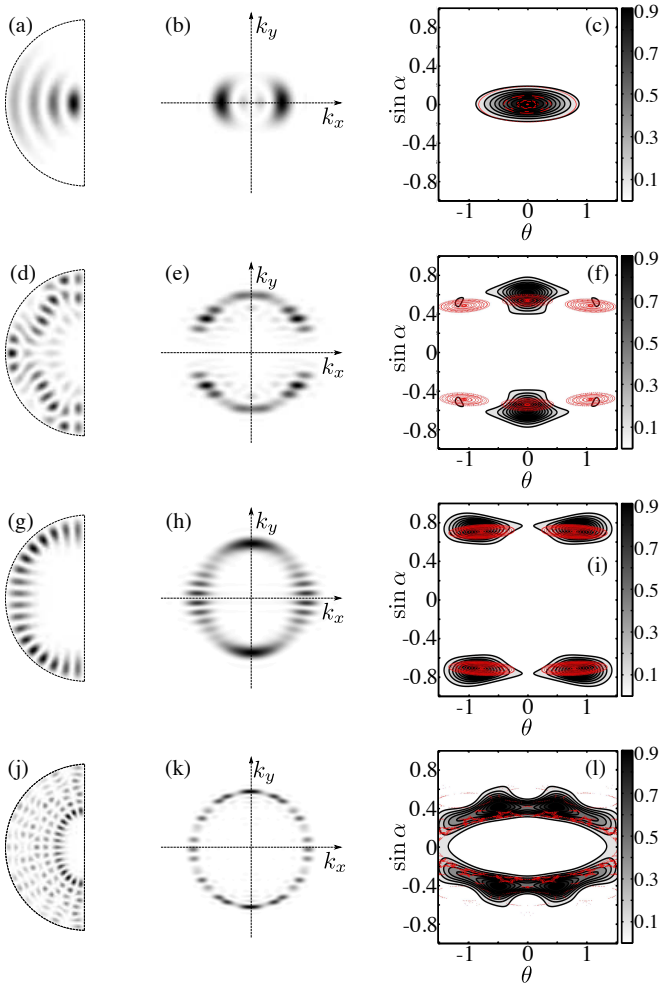

FIG. 3. Examples of modes of the mixed fiber with $\gamma = 0.95$: Near-field, Far-field and Husimi representation of (a,b,c) a regular mode of the 2-PO. Super-imposed in red is the PSS associated to the 2-PO ; (d,e,f) a mode built on the 5-PO. In red, the PSS of the 5-PO ; (g,h,i) a mode built on the 6-PO. In red the PSS of the 6-PO ; (j,k,l) a chaotic mode.

distribution $P(s_\Delta)$ in a mixed system is given by

$$P(s_\Delta) = \frac{d^2}{ds_\Delta^2}\left[\exp\left(-W s_\Delta\right)\,\mathrm{erfc}\left(\frac{\sqrt{\pi}}{2}\left(1-W\right)s_\Delta\right)\right] \tag{3}$$

where $0 < W < 1$ is the density of regular states. A formal evaluation of W is deduced directly from the PSS, by measuring the area of the regular region, weighted by the lengths of the associated trajectories. Figure 4 shows the statistics of a chaotic ($\gamma = 3/2$) and a mixed ($\gamma = 0.95$) cavity, respectively for symmetric [Fig. 4(a),(c)] and antisymmetric [Fig. 4(b),(d)] modes. The gray scale histograms represent the energy level spacing distribution calculated for a sample of 900 modes for each symmetry, with an avoidance of the first hundred modes. The red line is a fit of the histograms by the function $P(s_\Delta)$ (eq. (3) giving an estimation of the parameter W. For the chaotic case, $W = 0$ indicates that the relative size

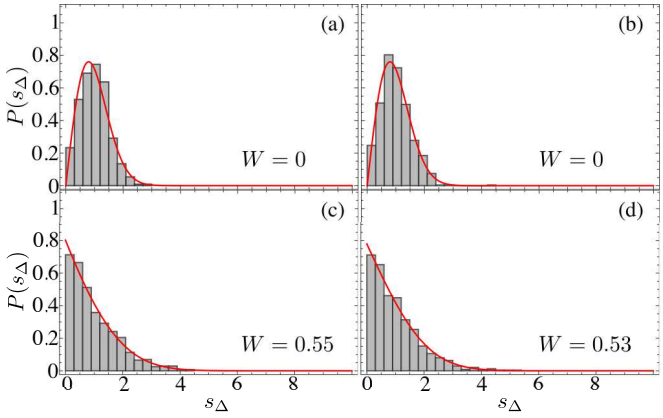

FIG. 4. Probability distribution of the energy level spacing for the symmetric and anti-symmetric modes of (a,b) a chaotic cavity ($\gamma = 3/2$) and (c,d) a mixed cavity ($\gamma = 0.95$).

of the regular region is reduced to zero. This result is consistent with the typical PSS of a chaotic system [Fig. 2(e)]. Indeed, the inherent nature of a chaotic dynamics is to avoid any stable structure. On the contrary, for the mixed system, $W \simeq 0.5$ corresponds to a PSS half-filled with the regular region. Note that this is qualitatively coherent with the PSS presented in Fig. 2(c). The case $W = 1$ would correspond to the regular systems $\gamma = 1$ (half-circle) and $\gamma = 2$ (circle).

III. REGULAR MODES AS MODES OF A PLANO-CONCAVE RESONATOR

As evidenced in details by H. E. Turecci in dielectric microcavities [24], the modes localized on stable POs can be described in terms of Gaussian optical theory. Using the standard description of optical resonators, we develop that correspondence for the 2-PO regular modes as the analogous of the fundamental longitudinal modes of a plano-concave optical resonator with dielectric boundaries where x acts as the longitudinal axis of propagation and y as the transverse direction. Both the stability of the cavity and the spatial field distribution of the modes of the fiber are thus analyzed.

First, the ray transfer matrix formalism enables to study the stability of the cavity by investigating the paraxial ray evolution in the vicinity of the 2-PO. Let (y, α) be the couple of quantities describing the position of a ray in the resonator, with y the position of the ray on the boundary (including the straight part). In the paraxial approximation, the output quantities are deduced from the input quantities using the relation:

$$\begin{pmatrix} y_{out} \\ \alpha_{out} \end{pmatrix} = M_t \begin{pmatrix} y_{in} \\ \alpha_{in} \end{pmatrix} \tag{4}$$

where M_t is the ray transfer matrix. The stability of the resonator is given by the value of the trace of M_t associated to a periodic sequence of a given ray. When

rays are periodically refocused, the sequence is stable and the geometric characteristics of the resonator obey:

$$0 < \left(1 - \frac{d}{R_1}\right)\left(1 - \frac{d}{R_2}\right) < 1 \tag{5}$$

where d represents the resonator length and R_1, R_2 are the radii of curvature of the resonator boundaries. This stability condition is analogous to the stability analysis of dynamical systems based on the evolution of a small deviation in the vicinity of a PO [36]. The transfer matrix is then formally equivalent to the so-called monodromy matrix.

In our case, $R_1 = a$ and $R_2 = \infty$ because of the flat reflective boundary. From the relation (5), one sees that the stability of the resonator depends on the value of d and thus of γ. Case $\gamma = 1$ is associated to the hemispheric stable resonator. For $1 < \gamma < 2$, the resonator is unstable. For $\gamma < 1$, the condition (5) is fulfilled so that the resonator is stable. Note that the case $\gamma = 2$ corresponds to $R_1 = R_2 = a$ and is associated to the concentric stable resonator. The mixed fiber with $\gamma = 0.95$ can thus be considered as a stable optical resonator whereas the chaotic fiber ($\gamma = 3/2$) corresponds to an unstable resonator [23, 34, 37].

In the following, we consider the case of the stable resonator with $\gamma = 0.95$, corresponding to the cross section of our actual optical fiber. We use the Gaussian wave formalism in the (x, y)-plane in order to study the spatial distribution of the modes built on the 2-PO. The spatial expansion of a beam traveling in the x-direction in the slowly varying envelope approximation reads:

$$\psi(x, y) = u(x, y)\, \exp\left(-j\kappa x\right) \tag{6}$$

with the phase varying mainly linearly in the x-direction and $\psi(x, y)$ being a solution of the transverse Helmholtz scalar equation $\Delta\psi + \kappa^2\psi = 0$. By using expression (6) for $\psi(x, y)$, one gets the following Fresnel (or parabolic) form for the wave equation in the paraxial approximation:

$$\frac{\partial^2 u}{\partial x^2} + \frac{\partial^2 u}{\partial y^2} - 2j\kappa\frac{\partial u}{\partial x} = 0 \tag{7}$$

Under the assumption of $u(x, y)$ varying slowly enough with x so that $|\partial^2 u/\partial^2 x| \ll |2\kappa\partial u/\partial x|$ and taking into account the curvature of the wave front imposed by the geometry of the cavity, the solution $u(x, y)$ of (7) is given by [38]:

$$u(x, y) = \frac{w_0}{w(x)} H_m\left(\sqrt{2}\frac{y}{w(x)}\right) \exp\left\{j\phi_t - y^2\left(\frac{1}{w^2(x)} + j\frac{\kappa}{2R(x)}\right)\right\} \tag{8}$$

where $w(x)$ is the beam radius, w_0 is the minimum beam diameter – the so-called waist diameter – for which the phase front is plane, $R(x)$ the radius of curvature of the wavefront and H_m is the Hermite polynomial of order m and ϕ_t a global phase described right below. The solution $u(x, y)$ is consistent with the theory of Gaussian beams along the y-direction [38]. The Gaussian beam profile is characterized by the beam radius $w(x)$. An initial Gaussian beam of width w_0 at $x = 0$ experiences a transverse expansion given by $w^2(x) = w_0^2\left(1 + (x/x_\mathrm{r})^2\right)$, where the Rayleigh length x_r measures the spatial coherence of the beam along the axis of propagation x. In our specific case, the relevant wavelength is the transverse wavelength $\lambda_\perp = 2\pi/\kappa$. Then, the Rayleigh length x_r and the beam waist w_0 are related through $x_\mathrm{r} = \kappa w_0^2/2$. The beam propagating along the 2-PO also undergoes a phase shift which is twofold. First, the reflection on the dielectric core/cladding interface – governed by Fresnel reflections laws – implies a phase shift ϕ_r^κ which depends on κ. Second, the Gouy phase ϕ_g [38, 39] appears when the beam focuses. It results in a complex total phase shift ϕ_t that reads :

$$\begin{aligned}\phi_t &= \phi_r^\kappa + \phi_g \\ &= 2\arctan\sqrt{(n_\mathrm{co}^2 - n_\mathrm{cl}^2)\, k_0^2/\kappa^2 - 1} \\ &\quad + (m+1)\arctan\sqrt{\frac{\gamma}{1-\gamma}}\end{aligned} \tag{9}$$

where $k_0 = 2\pi/\lambda_0$ is the modulus of the vacuum wavevector. Stationary modes occur when the accumulated phase shift along a round-trip in the resonator is a multiple of 2π. From (8) and (9), this condition of constructive interferences leads to:

$$\kappa_{m,p}\, 2d = 2\pi p + 2\phi_r^\kappa + 2(m+1)\arctan\sqrt{\frac{\gamma}{1-\gamma}} \tag{10}$$

Each mode of the resonator is then defined by the value of its transverse wave vector $\kappa_{m,p}$ which depends on two integers, m and p running from 0 to maximum values satisfying $\kappa_{m,p} < k_0\sqrt{(n_\mathrm{co}^2 - n_\mathrm{cl}^2)}$ [14]. In the optical resonator analogy, p defines the number of nodes along the axial direction x, that is the order of the longitudinal mode along the 2-PO, whereas m is the transverse mode number associated to the so-called high-order modes. The fundamental Gaussian mode, namely the fundamental mode for the transverse oscillations, corresponds to $m = 0$ and $p = 0$. A few examples of the modes of the fiber/resonator with their corresponding values of (m, p) are given in Figure 5.

IV. REGULAR MODES AS LOCALIZED MODES INDUCED BY THE MIXED DYNAMICS

The ergodic modes of a fully chaotic system stand for the generic behavior. They are characterized by Gaussian statistics of the spatial field distribution. Nevertheless, some modes, exhibiting an "*extra density (that)*

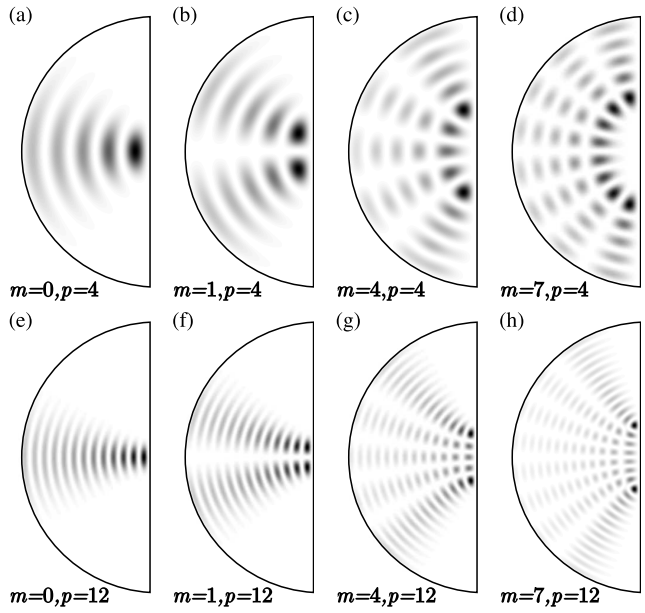

FIG. 5. Spatial distribution of intensity for modes of the mixed fiber ($\gamma = 0.95$) associated to different values of (m, p). (a)-(d) $p = 4$ and $m = 0, 1, 4, 7$, (e)-(h) $p = 12$ and $m = 0, 1, 4, 7$.

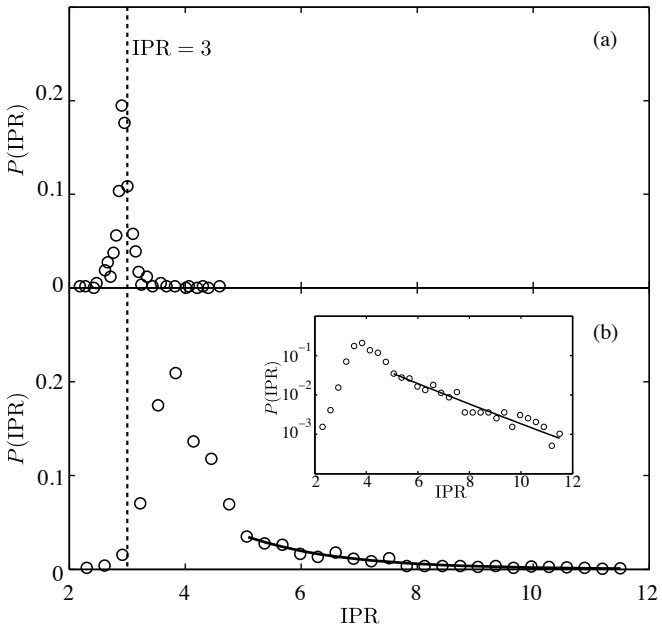

FIG. 6. Probability distribution of the Inverse Participation Ratio. (a) Chaotic cavity ($\gamma = 3/2$). The probability distribution is centered around the value IPR=3. (b) Mixed cavity ($\gamma = 0.95$) presenting some larger values of the IPR. The continuous line is a fit based on a nonlinear sigma model [41]. Inset : same as (b) in logarithmic scale.

surrounds the region of the periodic orbit" [40] are constructed along *unstable* periodic orbits. They are usually called "scar modes". Regular modes of a mixed system also result from constructive interferences with the main crucial difference that they take place along a *stable* periodic orbit. This intrinsic distinction in the nature of the underlying periodic orbit implies, among other features, a stronger spatial localization of the field [see for example Fig. 5(a) and (e)]. This localization implies a substantial deviation in the statistics compared to the homogeneous field distribution. The Inverse Participation Ratio (IPR) and its statistics, which are commonly used tools in the characterization of the spatial signatures of chaotic or disordered systems, highlight this localization feature. The IPR, that is the second order moment I_2 of the intensity, is also defined as :

$$I_2 = \frac{\frac{1}{\mathcal{S}} \iint_{\mathcal{S}} I^2(x,y) d\mathcal{S}}{\left(\frac{1}{\mathcal{S}} \iint_{\mathcal{S}} I(x,y) d\mathcal{S}\right)^2} \tag{11}$$

where $I(x, y) = |u(x, y)|^2$ is the field intensity, and $\mathcal{S}$ the surface of the transverse cross section of the fiber. The distribution of the IPR [Fig. 6] for the modes of the chaotic and mixed fibers exhibit some specific features. For the chaotic fiber ($\gamma = 3/2$), $P(I_2)$ presents a peaked distribution around the value $I_2 = 3$ [42, 43] as expected by the universal properties of ergodicity of the generic modes of a chaotic system [14]. Even if scar modes present some enhancement of intensity, this is marginal enough not to appear in the distribution of the IPR [Fig. 6(a)]. The Random Matrix Theory (RMT) predicts that there should be no fluctuations around 3, but as the system is bounded, fluctuations appear [41]. On the contrary, the distribution of IPR calculated for the modes of the mixed fiber shows an asymmetric profile with values higher than twice the actual mean value $\langle I_2 \rangle \simeq 4.5$. This points out that a large number of modes contributes to this deviation by presenting highly localized intensities. In disordered systems, this behavior is currently associated to the presence of so-called "localized modes" [22]: some theoretical studies based on the supersymmetry method [44] predict the asymmetry of the IPR distribution in the (Anderson) localization regime. The distribution of the IPR is then expected to follow :

$$P(I_2) = C \sqrt{\frac{g}{I_2}} \exp\left(-\frac{\pi}{6} g I_2\right) \tag{12}$$

for $I_2 \gg \langle I_2 \rangle$ where $\langle I_2 \rangle$ is the mean-value of the IPR, C is a normalization constant. In disordered systems, g is the conductivity that depends on the system size, $\langle I_2 \rangle$, and the mean-free-path [41]. The high values of I_2 in Fig. 6(b) present a very good agreement with eq. (12) with $g = 0.94$ and $C = 0.88$. This is confirmed by the inset of Fig. 6(b) which shows $P(I_2)$ in logarithmic scale. Thus, we get the same signature of spatial localization, as the one encountered for localized modes of disordered systems. Here, localization is the result of the stable dynamics.

To investigate the origin of this deviation in the tail of the IPR distribution, we report in Figures 7 and 8 the value of the IPR of each individual mode as a function

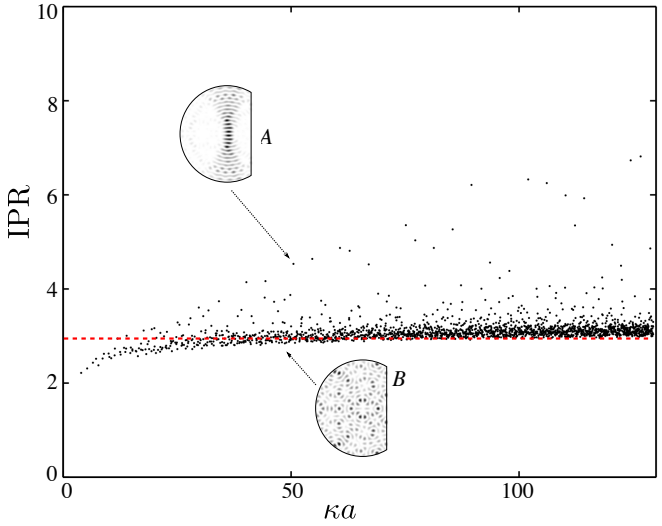

FIG. 7. Inverse Participation Ratio (IPR) as a function of the transverse wave number $\kappa\, a$ for the chaotic case ($\gamma = 3/2$) ; As expected, the IPR concentrates in the vicinity of IPR=3 except for the modes built on neutral orbits (upper inset, A). Inset B shows a generic ergodic mode.

of $\kappa\, a$ for the chaotic [Fig. 7] and mixed [Fig. 8] fibers. As expected for the chaotic case, the IPR tends to an asymptotic value of 3 for most of the modes. As exemplified by the ergodic mode presented in the inset B of Fig. 7, the wavefunction is statistically uniformly distributed over the fiber's cross section, thus resulting in Gaussian spatial statistics and an expected value of 3 for the IPR. The modes presenting larger values of the IPR [Fig. 7] are some specific spatially localized modes that concentrate on a region of the PSS surrounding continuous families of marginally unstable PO. These "bouncing ball" modes do not follow the standard Gaussian statistics and take place along the full diameter of the fiber [see inset A in Fig. 7].

Figure 8 presents the IPR as a function of $\kappa\, a$ for the modes of the mixed fiber. The main observation one can make at the first glance is a striking structuration of the values of the IPR for individual modes. More thoroughly, we have identified families of modes following a monotonous behavior. The upper red circles all correspond to the family of regular modes along the 2-PO. The high values of the IPR confirm a strong spatial localization of intensity of these modes, also labelled as the fundamental Gaussian modes $u_{0,p}$. The dots in shades of colors from red to green correspond to the IPR calculated for the higher order modes $u_{m,p}$ with m varying from $m = 1$ to $m = 9$. The regularity of the IPR as a function of $\kappa\, a$ is also observed for higher values of m whose maximum value $m_{\max}$ is given by $\kappa_{m_{\max},0} = k_0\sqrt{(n_{\rm co}^2 - n_{\rm cl}^2)}$. Nevertheless, they are not pointed out in the figure for the sake of clarity. The crosses in shades of blue correspond, as pointed out by the inset images labelled from A to E, to Whispering Gallery Modes (WGM) built upon quasi-periodic marginally stable orbits. The WGMs are localized on the boundaries of the cavity, so their IPR is expectedly higher than 3. The light blue crosses correspond to WGMs with a single crown (A), as the medium blue and dark blue crosses correspond respectively to WGMs with double (B) and triple (D) crowns. When the curves intersect, the corresponding WGMs are degenerated as shown for the modes C and E. The purple crosses correspond to the modes localized in the vicinity of the 6-bounce PO and follow a well-distinguished behavior as well. It is worth noting that for low values of $\kappa\, a$, the WGMs and the modes built upon the 6-PO are undistinguishable, which is visible for $\kappa\, a < 50$ as the medium blue and purple crosses are following the same evolution. All these modes contribute to the deviation of the IPR observed in Fig. 6(b). The parameter $g = 0.94$, evaluated by a fit of eq. (12) implies a "mean-free-path" $l \simeq 50\mu$m. This value is consistent with the order of magnitude of the distance between successive bounces of trajectories underlying the modes responsible for the deviation.

The modes corresponding to the lower IPRs – marked in black, right above IPR=3 (red dashed line) – correspond to chaotic modes that present an ergodic behavior. The density of points around IPR=3 is much less important than above, which confirms that ergodic modes are a minority in a mixed system characterized by the parameter $\gamma = 0.95$. This behavior of strong deviation from the standard value IPR=3 is commonly encountered is systems presenting a strong enough *disorder* to promote the existence of (Anderson-) localized modes. Here the *order*, by means of the regular modes, is responsible for the deviation of the IPR.

By use of a heuristic model, we derive an analytic expression for the value of IPR for the 2-PO regular modes with respect to κ. We assume that the modes are spatially localized on a surface $\mathcal{S}_{\rm loc}$. Thus, the intensity of each mode equals I_0 on $\mathcal{S}_{\rm loc}$, and 0 elsewhere. Then, with $I_0 = \mathcal{S}/\mathcal{S}_{\rm loc}$ and using equation (11), one gets:

$$I_2 = \frac{\mathcal{S}}{\mathcal{S}_{\rm loc}} \tag{13}$$

Using the analogy of these modes with the fundamental gaussian modes $u_{0,p}$ of the stable resonator (see section III), we derive an analytic expression for $\mathcal{S}_{\rm loc}$:

$$\begin{aligned}\mathcal{S}_{\rm loc} &= 2\int_0^d w(x)dx \\ &= 2w_0 x_{\rm r}\left(\frac{d}{x_{\rm r}}\sqrt{1+\left(\frac{d}{x_{\rm r}}\right)^2} + \operatorname{arcsinh}\left(\frac{d}{x_{\rm r}}\right)\right) \\ &= w_0 L_{\rm eff}\end{aligned} \tag{14}$$

where $L_{\rm eff}$ is an effective length associated to the regular modes. Finally, using the relation between x_r and κ one gets:

$$I_2 = \frac{\mathcal{S}\sqrt{\kappa}}{L_{\rm eff}\sqrt{2x_{\rm r}}} \tag{15}$$

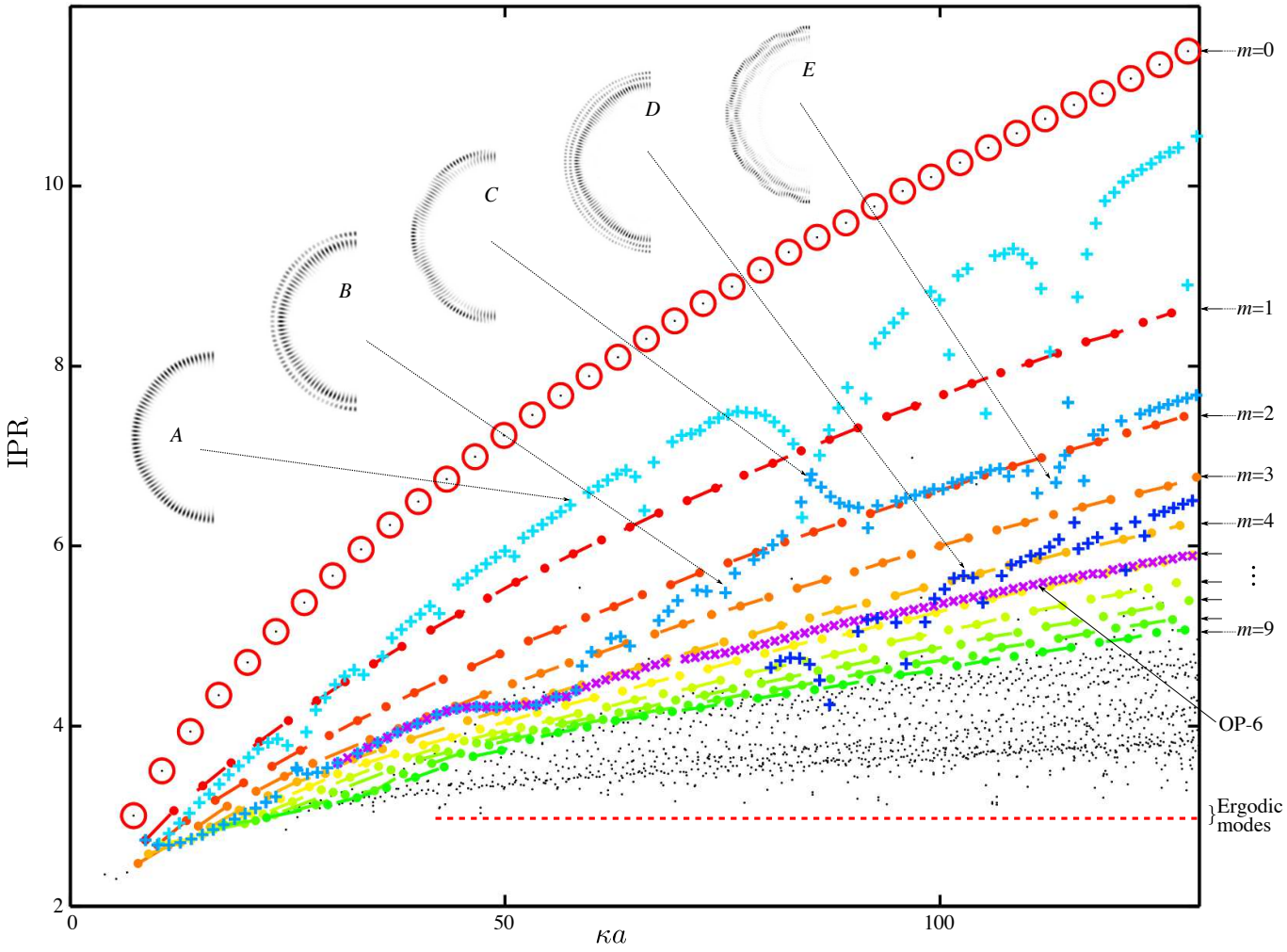

FIG. 8. Inverse Participation Ratio (IPR) as a function of the transverse wave number κa for the mixed case ($\gamma = 0.95$) ; Families of modes are distinguishable as shown by the different markers: red circles [○] correspond to 2-PO regular modes, from red to green dots [from • to •] correspond to higher order regular modes denoted from $m = 1$ to $m = 9$, purple crosses [×] correspond to modes built on the 6-PO, light, medium and dark blue crosses [+,+ and +] correspond to whispering gallery modes (insets A to E).

In our system, we evaluated x_r for the 2-PO regular/fundamental Gaussian modes, and checked that it does not depend on κ. So, the IPR varies proportionnally with $\sqrt{\kappa}$. We obtain a perfect agreement between expression (15) and the values of IPR for the 2-PO regular modes $u_{m=0,p}$ [large red circles and red continuous line in Fig. 9].

Moreover, for large values of κ, the IPR appears to structure itself by presenting a regular evolution for each family of modes $u_{m,p}$ with different m. The dots in shades of colors from red to green are the IPRs of high order modes for m ranging from 0 to 9 as shown in Fig. 8. The IPR for the modes of a given m value are following a monotonous curve which is perfectly adjusted by the empirical expression:

$$I_2^{u_{m,p}}(\kappa) = c_m \kappa^{\xi_m} \qquad (16)$$

where c_m is different for each m. The exponent ξ_m has a linear dependance with m which is $\xi_m = -0.017\,m + 1/2$. For $m = 0$, one recognizes the $\sqrt{\kappa}$ dependance predicted by eq. (15). In Figure 9, we mark the evolution of the IPR with m for three fixed p values (full blue circles). The IPR follows a decreasing curve as m increases and this behavior is encountered for all p values (even if we marked only three values in the figure for sake of clarity). Thus, we can assume that it exists a relation between the comportment of the IPR and the p and m integers that characterize the whole family of regular modes. Both this behavior and the previous empirical ansatz point out the tight relationship of the IPR for the family of the regular modes with the gaussian modes and will be the subject of further investigations.

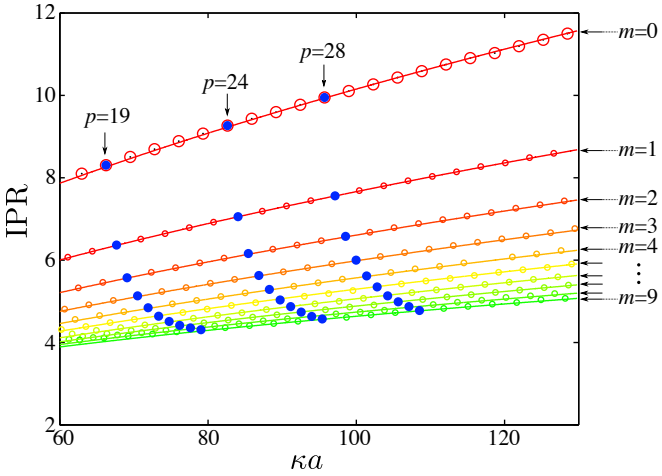

FIG. 9. IPR as a function of κa for the regular modes and for high values of κ. The dots and circles correspond to the points presented in Fig. 8 and the continuous lines correspond to the expression (16). The full circles point out the IPR for a fixed value of p while m varies from 0 to 9. Three values of p are marked.

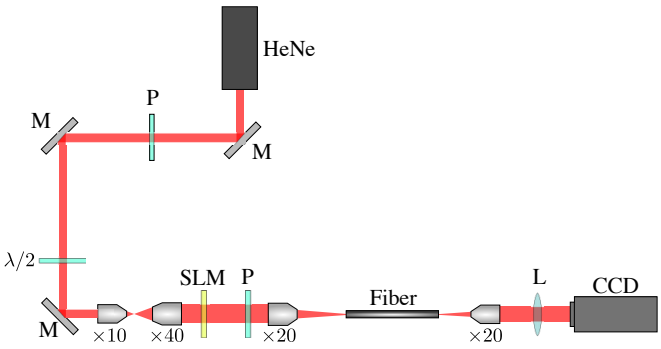

FIG. 10. Experimental setup. P: polarizer; M: mirror; $\lambda/2$: half-wavelength waveplate; ×10, ×20, ×40: microscope objectives; SLM: Spatial Light Modulator; L: lens needed to collect the FF; CCD: CCD camera.

V. EXPERIMENTAL OBSERVATION AND MANIPULATION OF THE REGULAR MODES OF THE MIXED FIBER

In order to study experimentally the light propagation into a mixed fiber, we manufactured a multimode optical fiber whose transverse shape is a truncated disk with $\gamma = 0.95$. The experimental setup is showed in Figure 10. The illumination is made with a 2mW HeNe cw laser ($\lambda_0 = 633$nm). The polarization is controlled through a polarizer and a $\lambda/2$ wave-plate. The transverse wavenumber of the initial beam with respect to the optical axis is controlled *via* the relation $\kappa = k_0 \sin\Theta$ with Θ the angle of the beam with respect to the optical axes. It fixes the average transverse wavenumber of the range of excited modes and thus to select the modes. An other way to control the modes' excitation is performed through the utilization of a Spatial Light Modulator (SLM, Amplitude only). A spatial modulation can be imposed through the SLM in order to shape the spatial distribution of the field intensity and then select a family of excited modes. At the output of the fiber, the intensity is collected by a microscope objective and imaged on a CCD Camera. The NF is then directly collected. A supplementary lens is needed in order to collect the FF.

A. Rough selection of 2-PO regular modes by a focused beam

At first, we did not use the SLM, and we only control the illumination by the position and the angle of a focused beam in front of the input end of the fiber. Figures 11(a) and (g) show two typical illuminations. A gaussian beam on the fiber input is obtained at the focal point of a microscope objective, and a tilt is given in order to select the range of transverse wave vectors propagating into the fiber. Figure 11(b) presents the NF measured at the fiber's output for the first illumination [Fig. 11(a)]. The spatial distribution of the NF is characteristic of a superposition of regular modes of the 2-PO. One can observe both a concentration of intensity near the straight boundary and a confinement of intensity close to the 2-PO which are a signature of the 2-PO regular modes. Indeed, all the regular modes along the 2-PO present such an enhancement of intensity in the vicinity of the x-axis. Moreover, one can note the circular arc-like pattern also present on Figures 5(a) and (e). Figure 11(c) exposes the FF intensity pattern of the outgoing waves. The anisotropic configuration along the κ_x-axis confirms that the field builds up on the 2-PO. The κ_x broadening testifies that numerous gaussian-like modes of the type $u_{0,p}(x,y)$ have been excited. We note also that unlike the FF of an individual 2-PO regular mode, the figure is asymetric along κ_y. This is due to a slight displacement of the initial beam along the y-axis.
Figures 11(d) and (e) show the NF and FF resulting from numerical simulations. Using a standard beam propagation method algorithm [45], we simulate the propagation of an initial gaussian beam along the optical fiber. The parameters here are given in order to reproduce the experimental initial condition. As one can see, the resulting patterns reproduce in the NF as well as in the FF the experimental observations and validate our description of the experiments. Moreover, it permits to get more informations on the modes that contribute to the observed field. Figure 11(f) presents the numerical spatial frequency spectrum $|\tilde{\mathcal{C}}(\kappa)|$ calculated through the standard method [46]. More precisely, $|\mathcal{C}(\kappa)|$ is the modulus of the Fourier transform of the correlation function $\tilde{\mathcal{C}}(z)$ defined as the overlap between the outgoing field and the initial condition. First, the observed Fabry-Perot-like spectrum confirms that the analogy between the 2-PO regular modes of the mixed fiber and the gaussian modes of a

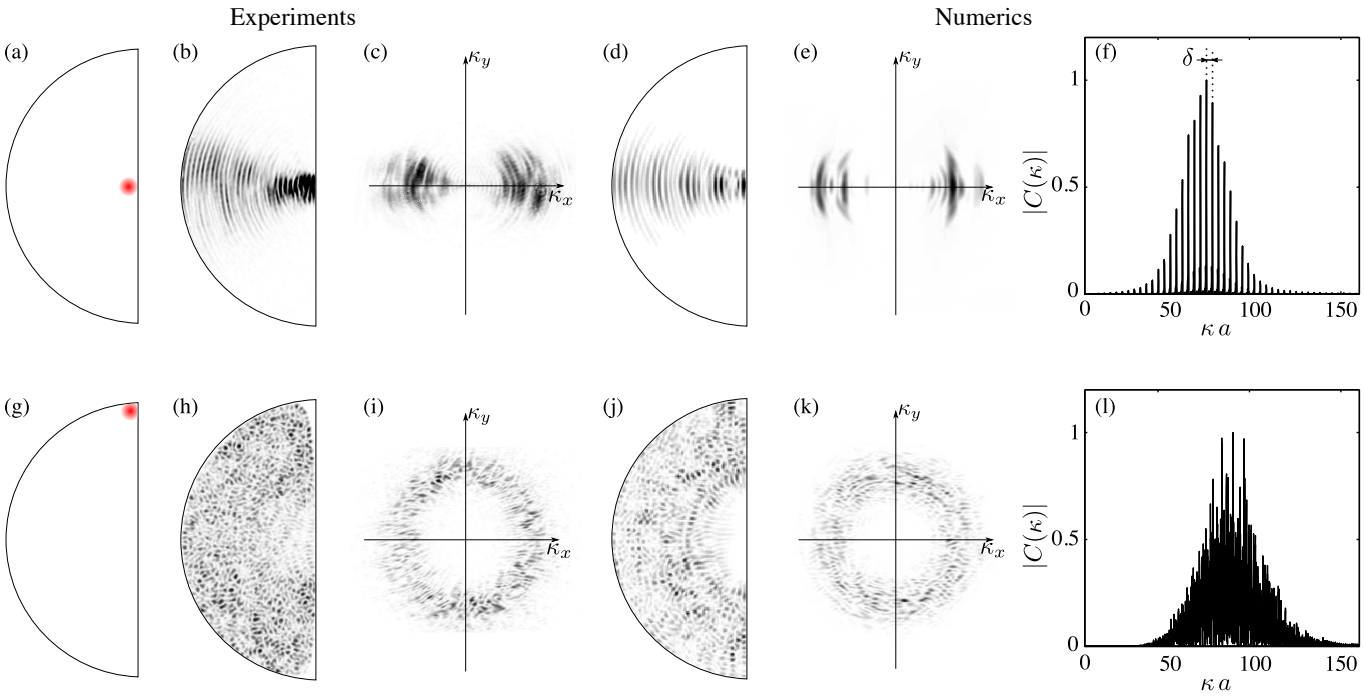

FIG. 11. Initial illumination beams, NF and FF observed at the output of the fiber, corresponding numerical simulations and numerical calculated spectra, for an illumination favorable to the excitation of a family of (a-f) regular modes and (g-l) superposition of modes with no 2-PO regular modes.

stable optical cavity is relevant. Each peak corresponds to a value of κ associated to a 2-PO regular modes and can be labelled by different p values. We measure a free spectral range $\delta \approx 3.3$ which is consistent with the theoretical free spectral range for the modes along the 2-PO, $\delta = (\Delta\kappa)\, a = \pi a/d = \pi/\gamma$ where $\Delta\kappa = \kappa_{m,p+1} - \kappa_{m,p}$ as defined in equation (10). In figure 12, we perform a zoom on the spectrum between two adjacent peaks associated to $p = 21$ and $p + 1 = 22$. Secondary peaks appear systematically close to each primary peaks associated to 2-PO regular modes. They correspond to high-order transverse modes that have a good overlap with the initial beam focused along the symmetry axis of the fiber in the vicinity of the truncation.

We indicate a peak associated to the 2-PO regular mode $u_{0,21}$ in Figure 12. At a distance Δ of this peak, we point a peak with lower amplitude which correspond to a transverse mode with the same p but with $m = 2$, $u_{2,21}$. As the value of $\kappa_{2,p} > \kappa_{0,p}$, this peak is actually closer to the peak corresponding to the 2-PO mode $u_{0,p+1=22}$ than $u_{0,21}$. We measure the interval Δ between the values of $\kappa\, a$ for $u_{0,21}$ and $u_{2,21}$. Following eq. (10), we expect to get

$$\Delta = \frac{2}{\gamma} \arctan \sqrt{\frac{\gamma}{1-\gamma}} + \delta\phi_r = 2.84 \qquad (17)$$

where $\delta\phi_r$ is the difference between the phase shift $\phi_r^{\kappa_{0,p}}$ and $\phi_r^{\kappa_{2,p}}$ which is negligible. The measured value $\Delta = 2.84$ confirmed the identification of the peaks.

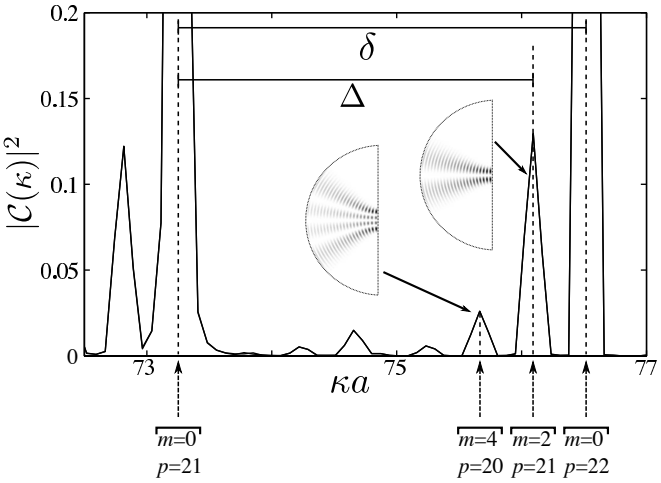

FIG. 12. Zoom of the spectrum of Fig. 11(f) between two peaks $p = 21$ and $p = 22$. In inset, the intensity of the modes corresponding to $u_{4,20}$ and $u_{2,21}$.

The peak with lower amplitude on the left of the $u_{2,21}$ peak corresponds to $m = 4$ but for $p - 1 = 20$. In the same way, we measure $\Delta' = \kappa_{4,20}\, a - \kappa_{0,20}\, a = 5.69$ which is in agreement with the expected theoretical value $\Delta' = 4/\gamma \arctan \sqrt{\gamma/(1-\gamma)} + \delta\phi'_r = 5.68$, with $\delta\phi'_r = \phi_r^{\kappa_{4,20}} - \phi_r^{\kappa_{0,20}}$.

These secondary peaks correspond to transverse modes with even m. The maximum of intensity of modes with even $m > 2$ is not along the x-axis, therefore their weights

in the spectrum is very low. However, the modes with odd m present a zero of intensity along the symmetry axis and consequently have a poor overlap with the given illumination (see figure 5(b,f,d and h)).

Figure 11(h) presents the NF collected for the second illumination [Fig. 11(g)] that is for a beam focused far from the location of the 2-PO regular modes. Here, the pattern is completely different and the spatial distribution of intensity is statistically uniform, made of grains of light of random amplitude and size. This speckle-like pattern results from the superposition of a great number of modes including ergodic modes [see Fig. 3(j)]. The FF [Fig. 11(i)] confirms this assumption, by presenting an isotropic distribution of wavevectors whose moduli are radially confined around an average wavenumber $\bar{\kappa}$. The associated numerical simulations [figures 11(j) and (k)] reproduce the experimental results. The numerical spatial frequency spectrum [Figure 11(l)] does not present any predominant structuration: all the modes in the range of κ corresponding to the illumination are excited. The three regularly-spaced peaks one can see around $\kappa\, a = 90$ are a reminiscence of a regular modes along a periodic orbit that have been excited. The presence of zero-intensity area visible on Figure 11(j) underlines the fact that no 2-PO regular modes are excited (as those modes present a maximum of intensity in this location).

From the transverse wavenumber spectra, we aim to extract some informations on the underlying geometrical signature of the excited modes. A relevant way to characterize the presence or not of any regularity in the underlying ray dynamics is to calculate the Fourier transform of $|\tilde{\mathcal{C}}(\kappa)|$:

$$\mathcal{L}(\ell) = \int_0^{\kappa_{max}} d\kappa\, |\tilde{\mathcal{C}}(\kappa)| \exp\left(-j\kappa\ell\right) \qquad (18)$$

This *length spectrum* $\mathcal{L}(\ell)$ will display peaks at the corresponding orbit length. Thus, the geometrical length of the periodic orbits can be directly extracted from the measure of the spectrum $|\tilde{\mathcal{C}}(\kappa)|$ which is calculated independently from the knowledge of the underlying periodic orbits [47].

Figure 13(a) presents the length spectrum calculated from Fig. 11(f). The first peak corresponds to the length of the 2-PO (pointed out by the red arrow), that is $\ell/a = 2\,\gamma = 1.9$ (the factor 2 appearing for the round trip) and the other peaks being the harmonics. It is thus obvious that the only contribution to the spatial distribution of the field is due to a superposition of regular modes along the 2-PO. Figure 13(b) shows the length spectrum associated to the spectrum of Fig. 11(l) with the same scale as the latter. As shown in the inset, some peaks still appear as residual resonances not predominant in the dynamics. We point a peak corresponding to the 5-PO. The three regularly-spaced peaks on the spectrum [Fig. 11(l)] are associated to the 5-PO regular modes [see Fig. 3(d)]. We also report the position of the 2-PO length and note that no peak appears. The 2-PO doesn't contribute to the modes excited out of the symmetry axis of the fiber.

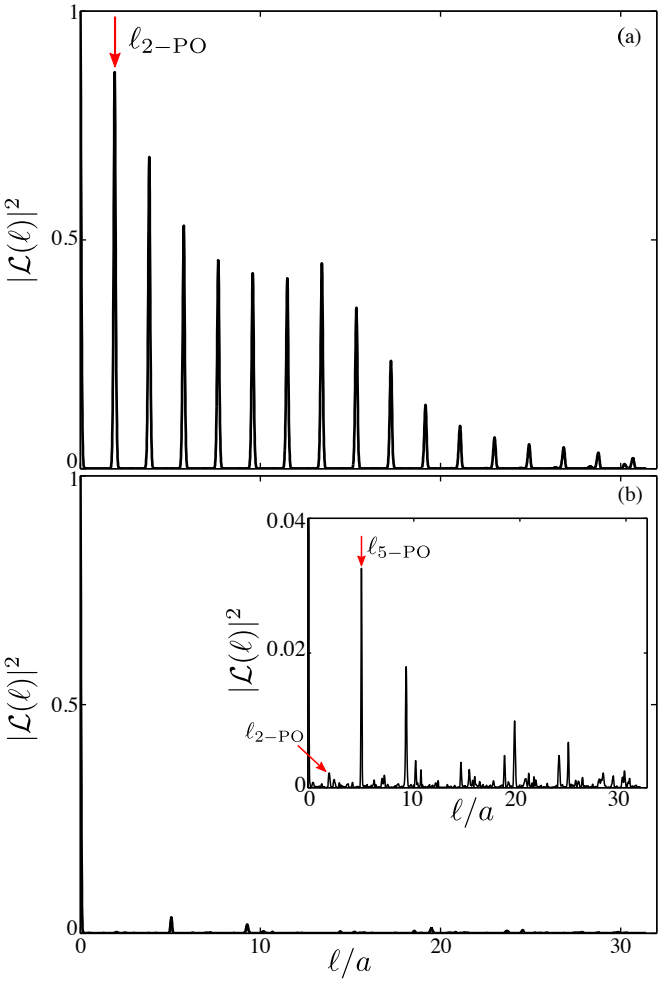

FIG. 13. Length spectra corresponding to spectra presented in (a) Fig. 11(f): one can see the regularly distributed peaks corresponding for the first to the length of the 2-PO and for the others to the harmonics ; and in (b) Fig. 11(l): one can see that no specific length exists (see inset) even if a zoom shows some peaks distributed in a disordered way. The arrows point the 2-PO and 5-PO respectively.

B. Fine selection of 2-PO regular modes by a modulated beam

As shown right above, a beam focused close to the truncation leads to the excitation of 2-PO regular modes due to a maximized overlap with the location of the gaussian transverse mode waists. The width of the spectrum (the number of excited modes) then depends on the size of the illumination beam. To control the excitation of 2-PO regular modes, we use a SLM to obtain a fine tuning of the illumination. We add a spatial modulation along the x-axis to select a direction of the transverse wave vector that matches those of the 2-PO regular modes. Moreover, we stretch the beam's transverse profile along the x-direction to optimize the overlap with the desired modes. Indeed, the propagating field $\psi(x, y, z)$ is the result of a superposition of the individual modes $\phi_n(x, y)$

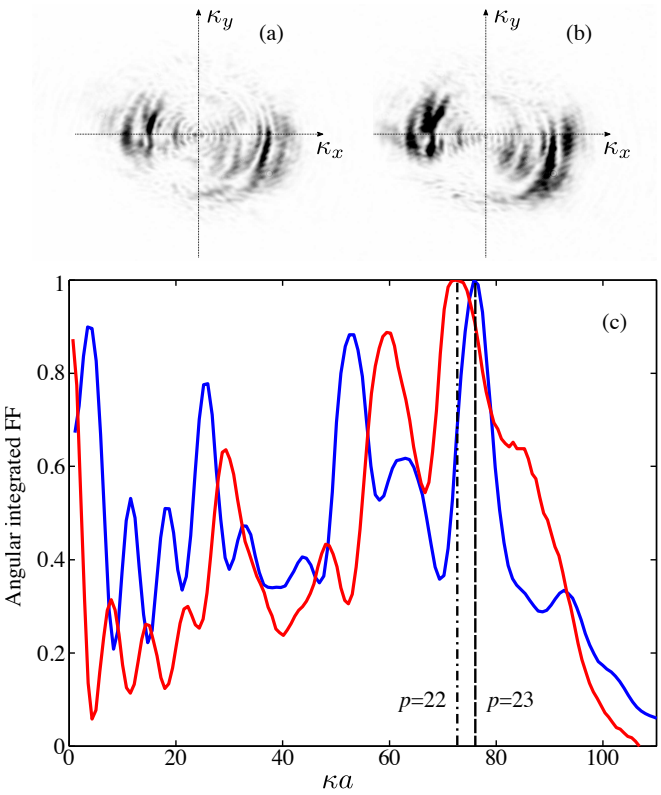

FIG. 14. (a,b) Experimental FF measured for two different spatial modulations of the illumination beam. (c) Angular integrated FFs. Blue line corresponds to case (a) and red line to case (b).

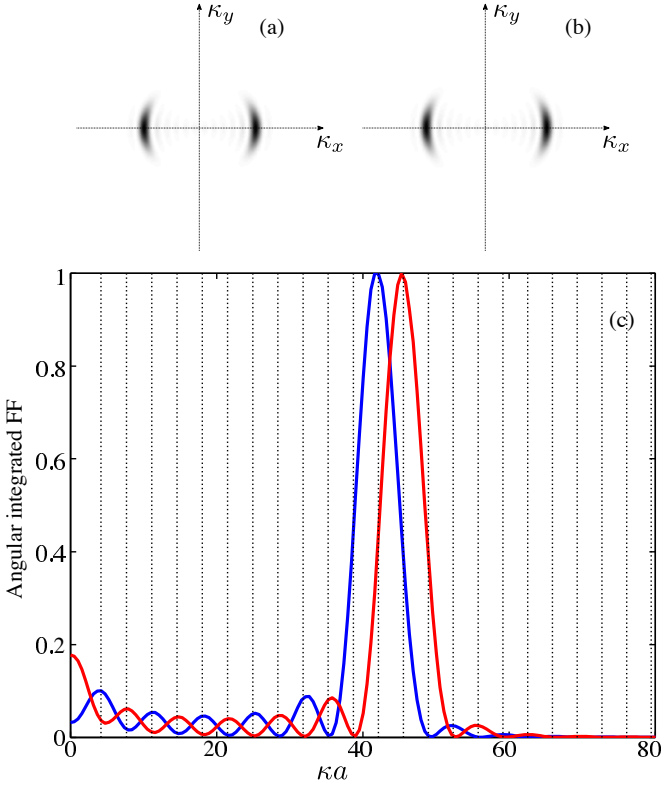

FIG. 15. (a,b) Numerical FF calculated for two different 2-PO regular modes with $p = 12$ and $p = 13$ respectively. (c) Angular integrated FFs. Blue line corresponds to case (a) and red line to case (b). The vertical dashed lines correspond to the value of the wavenumber of the $u_{0,p}$ modes.

written as :

$$\psi(x, y, z) = \sum_n c_n \phi_n(x, y) \exp(-j\beta_n z) \qquad (19)$$

where $\beta_n = \sqrt{k_0^2 - \kappa_n^2}$ is the constant of propagation of mode ϕ_n and $c_n = \iint d\mathcal{S}\, \phi_n(x, y)\psi^*(x, y, z = 0)$, is the weight of each individual mode in the superposition. Figures 14(a, b) show examples of the FF for two slightly different modulations – fixed *via* the SLM – associated to transverse wavenumbers κ of successive regular modes $u_{0,p}$ and $u_{0,p+1}$. To get rough informations on the transverse wavenumbers characterizing the propagated field, we calculate the angular integration of the far-field $|\tilde{\psi}(\kappa, \varphi, z)|^2$ [Fig. 14(c)]:

$$I_\kappa(\kappa, z) = \frac{1}{2\pi} \int_0^{2\pi} d\varphi\, |\tilde{\psi}(\kappa, \varphi, z)|^2 \qquad (20)$$

It is equivalent to a low-resolution spatial frequency spectrum due to smoothing induced by the Fourier transform of the individual modes and the interferences between the modes. The blue line (resp. red line) corresponds to the FF presented in Fig. 14(a) (resp. (b)).

In Figure 14, regularly spaced circle arcs clearly appear in the κ_x-direction in the FFs and correspond to the peaks observed in their angular integrations. It points out that only 2-PO modes have been selected. The highest peaks around $\kappa\, a = 76$ correspond to the value of κ fixed by the modulation. They are associated to two successive 2-PO regular modes with $p = 22$ for the red curve and $p = 23$ for the blue one. The peaks located around $\kappa\, a = 60$ testify on the excitation of lower order 2-PO regular modes as well, due to their good overlap with the initial condition. For low $\kappa\, a$ values, we observe some peaks that can be understood within the angular integration of the FF of individual regular modes.

In Figure 15, we report the angular integrated far-fields for two calculated individual 2-PO regular modes with consecutive p values, $p = 12$ and $p = 13$. To begin with, we observe that the curves present a peak at the expected position of the κ that are $\kappa_{0,12}\, a = 42.12$ and $\kappa_{0,13}\, a = 45.54$. We note also the presence of peaks with reduced amplitudes at the location of lower $\kappa\, a$ corresponding 2-PO regular modes. The occurence of these peaks is a consequence of the gaussian beam nature of the 2-PO regular modes along the stable trajectory. Those peaks would not appear for instance in the angular integration of the FF of the ergodic modes (as the one shown in Fig. 3(j)).

We perform numerical simulations to analyze the experimental angular far-field integration of Figure 14.

First an initial beam analogous to the one used in the experiment – that is an asymmetric gaussian beam stretched and modulated in the x-direction – is used on the one hand as initial illumination condition in the BPM algorithm. On the other hand, we evaluate the spatial overlap of this initial condition with the calculated modes to get the weights c_n of each individual mode in the propagating field $\psi(x, y, z)$. Numerically, we superimpose the angular integrated far-field resulting from the BPM simulation with the calculated weights $|c_n|$ of each mode. Figure 16(a) shows a behavior analogous to the experimental angular integrated far-field [Fig. 14(c)-red curve]. For low values of $\kappa\, a$, we observe some peaks pointed by the vertical arrows also detected on the experimental figure [see Fig. 14] that correspond to values of $\kappa\, a$ for $p = 2, 4, 6$. They constitute a direct signature of the Gaussian modes as shown in the integrated far-field of individual modes [Fig. 15]. We also observe two broad peaks in the integrated FF around $\kappa\, a = 40$ and $\kappa\, a = 50$. These large peaks result from the interferences between the excited modes preferentially being 2-PO regular modes. Indeed, by considering the value of $|c_n|$, we notice that modes with highest value of $|c_n|$ are the 2-PO modes (labelled by dashed vertical lines).
Finally, we report in Fig. 16(b), the angular integrated far-field for an initial modulated beam out of the 2-PO direction (precisely, in the upper part of the fiber, with a modulation having the same κ value but along the y-direction to avoid the 2-PO). We observe the vanishment of the first peaks associated to the characteristic signature of the 2-PO regular modes and an enlarged peak that corresponds to a superposition of a great number of arbitrary excited modes around the main κ value. The reported $|c_n|$ values show that a large amount of not identifiable modes are effectively excited.

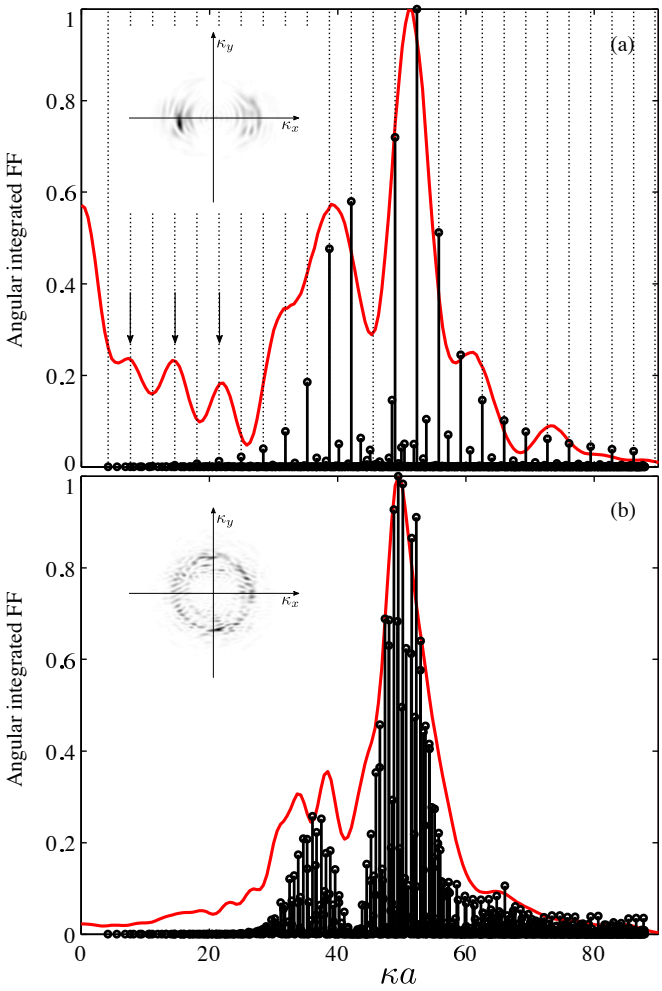

FIG. 16. Angular integrated FF obtained by numerical simulations. (a) For an illumination favorable to the excitation of regular modes. The vertical dashed lines correspond to the value of the wavenumber of the $u_{0,p}$ modes ; (b) For a modulation along the y-direction, so that no regular mode is being excited. The $|c_n|^2$ are represented by continuous dark lines in both cases. Insets show the corresponding FF.

VI. CONCLUSION AND DISCUSSION

In this paper we have presented numerical and experimental investigations of the modes of a highly multimode fiber whose transverse cross section is designed to induce complex ray dynamics. This system is versatile in the sense that a slight change in the level of the truncation leads to the exploration of different types of dynamics. One thus has access, with the same experimental system, to mixed, regular as well as chaotic dynamics. Here, we focused our work on the study of a mixed dynamics. After a brief review of the basics of dynamical systems as well as the analogy between the fiber's modes and Gaussian modes of an optical resonator, we concentrated our study on the deviation of the statistics of some family of modes from the generic behavior. The strong spatial localization of the regular modes finds remarkable signatures in the study of the IPR. By largely exceeding the value of the IPR predicted by the Random Matrix Theory, the regular modes of the mixed optical fiber present features commonly encountered in disordered systems exhibiting Anderson localized modes. Moreover, coupling these results with the analogy with the gaussian modes allowed us to derive an analytic expression for the IPR as a function of the wavenumber for the regular modes.

With a suitable shaping of the initial beam, we experimentally demonstrated that these modes can be selectively excited, and that they are robust to mode coupling. We analyse our results by means of the spectra, length spectra and angular integration of the output far-field, for any given initial illumination. This ease of shielding the other modes opens the way to multiple applications in optical telecommunications. For instance, the regular modes of the mixed optical fiber appear to be suitable for mode division multiplexing and would increase the number of transmission channels compared to the actual achievement available in conventional devices. Moreover, these modes can benefit

from a selective optical amplification, by optimizing the spatial overlap with a gain medium. To do so, one simply has to locate the active medium in the vicinity of the truncation, where the regular modes have their maximum of intensity [17]. In a more fundamental point of view, a nonlinear mixed optical fiber would promote an enhancement of the phenomenon of optical thermalization and condensation of classical waves, as the spatial overlap between the modes is an important parameter [48].

The authors thank gratefully M. Udé and S. Trzesien for their involvement in the preform and fiber manufacturing.

[1] H. Cao and J. Wiersig, RMP **87**, 61 (2015).
[2] H.-J. Stöckmann, *Quantum chaos: an introduction* (Cambridge University Press, 1999).
[3] A. Shnirelman, Usp. Math. Nauk. **29** (1974).
[4] M. V. Berry, J. Phys. A. Math. Gen. **10**, 2083 (1977).
[5] C. Gmachl, F. Capasso, E. Narimanov, J. Noeckel, A. Stone, J. Faist, D. Sivco, and A. Cho, Science **5**, 1556 (1998).
[6] T. Harayama and S. Shinohara, Laser Photonics Rev. **5**, 247 (2011).
[7] L. Ge, R. Sarma, and H. Cao, Optica **2**, 323 (2015).
[8] P. Aschiéri and V. Doya, JOSA B **30**, 3161 (2013).
[9] S. Tomsovic and D. Ullmo, PRE **50**, 145 (1994).
[10] A. Bäcker, R. Ketzmerick, S. Löck, J. Wiersig, and M. Hentschel, PRA **79**, 063804 (2009).
[11] S. Löck, A. Bäcker, R. Ketzmerick, and P. Schlagheck, PRL **104**, 114101 (2010).
[12] S. Gehler, S. Löck, S. Shinohara, A. Bäcker, R. Ketzmerick, U. Kuhl, and H.-J. Stöckmann, PRL **115**, 104101 (2015).
[13] Q. Song, S. Liu, Z. Gu, N. Zhang, and S. Xiao, Opt. Lett. **39**, 1149 (2014).
[14] V. Doya, O. Legrand, F. Mortessagne, and C. Miniatura, PRE **65**, 056223 (2002).
[15] V. Doya, O. Legrand, F. Mortessagne, and C. Miniatura, PRL **88**, 014102 (2001).
[16] C. Michel, V. Doya, S. Tascu, W. Blanc, O. Legrand, and F. Mortessagne, Appl. Opt. **48**, G163 (2009).
[17] C. Michel, S. Tascu, V. Doya, P. Aschiéri, W. Blanc, O. Legrand, and F. Mortessagne, PRE **85**, 047201 (2012).
[18] V. Doya, O. Legrand, and F. Mortessagne, Opt. Lett. **26**, 872 (2001).
[19] P. Leproux, V. Doya, P. Roy, D. Pagnoux, F. Mortessagne, and O. Legrand, Opt. Com. **218**, 249 (2003).
[20] Y. Jeong, J. Sahu, D. Paine, and J. Nilsson, Opt. Exp. **12**, 6088 (2004).
[21] D. Richardson, J. Fini, and L. Nelson, Nature Photonics **7**, 354 (2013).
[22] A. Lagendijk, B. Van Tiggelen, and D. Wiersma, Phys. Today **62**, 24 (2009).
[23] S. Ree and L. Reichl, PRE **60**, 1607 (1999).
[24] H. Tureci, H. Schwefel, A. Stone, and E. Narimanov, Opt. Express **10**, 752 (2002).
[25] C. Michel, V. Doya, O. Legrand, and F. Mortessagne, PRL **99**, 224101 (2007).
[26] P. Kŏska, P. Peterka, and V. Doya, (accepted in JSTQE).
[27] A. Ghatak and K. Thyagarajan, *An Introduction to Fiber Optics* (Cambridge University Press, Cambridge, UK, 1998).
[28] I. Percival, J. Phys. B At. Mol. Phys. **6**, L229 (1973).
[29] K. Husimi, Proc. Phys. Math. Soc. Jpn. **22** (1940).
[30] G. Birkhoff, in *Dyn. Syst.* (Cambridge, USA, 1927).
[31] B. Crespi, G. Perez, and S.-J. Chang, PRE **47** (1993).
[32] A. Bäcker, S. Fürstberger, and R. Schubert, PRE **70**, 036204 (2004).
[33] R. Balian and C. Bloch, Ann. Phys. (N. Y). **63** (1971).
[34] M. V. Berry and M. Robnik, J. Phys. A. Math. Gen. **17**, 2413 (1984).
[35] T. Rudolf, N. Mertig, S. Löck, and A. Bäcker, PRE **85**, 036213 (2012).
[36] M. V. Berry, Eur. J. Phys. **2**, 91 (1981).
[37] E. Bogomolny, Phys. D Nonlinear Phenom. **31**, 169 (1988).
[38] H. Kogelnik and T. Li, Appl. Opt. **5**, 1550 (1966).
[39] S. Feng and H. Winful, Opt. Lett. **26**, 485 (2001).
[40] E. Heller, PRL **53**, 1515 (1984).
[41] P. Pradhan and S. Sridhar, PRL **85**, 2360 (2000).
[42] A. Kudrolli, V. Kidambi, and S. Sridhar, PRL **75**, 822 (1995).
[43] P. Pradhan and S. Sridhar, J. Phys. **58**, 333 (2002).
[44] V. Prigodin and B. Altshuler, PRL **80**, 1944 (1998).
[45] M. Feit and J. Fleck, Appl. Opt. **17**, 3990 (1978).
[46] M. Feit and J. Fleck, Appl. Opt. **19**, 2240 (1980).
[47] M. Lebental, N. Djellali, C. Arnaud, J. S. Lauret, J. Zyss, R. Dubertrand, C. Schmit, and E. Bogomolny, PRA **76**, 023830 (2007).
[48] P. Aschieri, J. Garnier, C. Michel, V. Doya, and A. Picozzi, PRA **83**, 033838 (2011).